



LAWRENCE
LIVERMORE
NATIONAL
LABORATORY

FY04&05 LDRD Final Report Fission Fragment Sputtering

B. Ebbinghaus, T. Trelenberg, T. Meier, T. Felter,
J. Sturgeon, A. Kuboda, B. Wolfer

March 13, 2006

Disclaimer

This document was prepared as an account of work sponsored by an agency of the United States Government. Neither the United States Government nor the University of California nor any of their employees, makes any warranty, express or implied, or assumes any legal liability or responsibility for the accuracy, completeness, or usefulness of any information, apparatus, product, or process disclosed, or represents that its use would not infringe privately owned rights. Reference herein to any specific commercial product, process, or service by trade name, trademark, manufacturer, or otherwise, does not necessarily constitute or imply its endorsement, recommendation, or favoring by the United States Government or the University of California. The views and opinions of authors expressed herein do not necessarily state or reflect those of the United States Government or the University of California, and shall not be used for advertising or product endorsement purposes.

Auspices Statement

This work was performed under the auspices of the U. S. Department of Energy (DOE) by the University of California, Lawrence Livermore National Laboratory (LLNL) under Contract No. W-7405-Eng-48. The project (04-ERD-026) was funded by the Laboratory Directed Research and Development Program at LLNL.

Table of Contents

Abstract	4
Introduction	4
Background	5
Approach	8
Experimental Studies	8
A. Reactor Irradiations	8
B. Accelerator Experiments	13
Modeling Studies	17
A. Kinetic Energy of the Sputtered Material	17
B. Theory of Energy and Momentum Distribution	20
C. Impact Produced by Energetic Ions on Matter	21
D. Energy Deposition by Secondary Electrons	23
E. Impulse Deposition by Secondary Electrons	26
F. Monte-Carlo Simulations of Energy Transport	28
Exit Plan/Summary	28
References	29

FY04&05 LDRD Final Report
Fission Fragment Sputtering
LDRD Project Tracking Code: 04-ERD-026
Bartley B. Ebbinghaus, Principal Investigator

Abstract

Fission fragments born within the first 7 μm of the surface of U metal can eject a thousand or more atoms per fission event. Existing data in the literature show that the sputtering yield ranges from 10 to 10,000 atoms per fission event near the surface, but nothing definitive is known about the energy of the sputtered clusters. Experimental packages were constructed allowing the neutron irradiation of natural uranium foils to investigate the amount of material removed per fission event and the kinetic energy distribution of the sputtered atoms. Samples were irradiated but were never analyzed after irradiation. Similar experiments were attempted in a non-radioactive environment using accelerator driven ions in place of fission induced fragments. These experiments showed that tracks produced parallel to the surface (and not perpendicular to the surface) are the primary source of the resulting particulate ejecta.

Modeling studies were conducted in parallel with the experimental work. Because the reactor irradiation experiments were not analyzed, data on the energy of the resulting particulate ejecta was not obtained. However, some data was found in the literature on self sputtering of ^{252}Cf that was used to estimate the velocity and hence the energy of the ejected particulates. Modeling of the data in the literature showed that the energy of the ejecta was much lower than had been anticipated.

A mechanism to understand the nature of the ejecta was pursued. Initially it was proposed that the fission fragment imparts its momenta on the electrons which then impart their momenta on the nuclei. Once the nuclei are in motion, the particulate ejecta would result. This initial model was wrong. The error was in the assumption that the secondary electrons impart their momenta directly on the nuclei. Modeling and theoretical considerations showed that the secondary electrons scatter many times before imparting all their momenta. As a result, their energy transfer is more isotropic than directional. It was therefore concluded that the nuclei are set in motion not by direct collisions with the secondary electrons, but by repulsive forces caused by the temporary net positive local charge of the nuclei. This is caused by ejected electrons and by the reduced bonding nature of the nuclei caused by many of the local electrons being in excited and in non-bonding states.

Introduction

The energy loss of charged particles passing through matter has been a prominent research topic in nuclear physics and attracted the attention of some of the most illustrious physicists of the last century. As a result, a comprehensive understanding of the fundamental aspects for the slowing-down of charged particles in matter seems to

have been achieved long ago, although many details remain to be explored. Nevertheless, recent experimental results have revealed that high-energy heavy ions exert a mechanical action on the slowing-down medium that is not yet understood [1]. Whatever this action is, it manifests itself in different ways. One effect is the formation of particulate ejecta when a high-energy heavy ion traverses a thin solid film. Another phenomenon is the Klamünzer effect or the “Ion-irradiation induced anisotropic plastic deformation.” [2,3] Here, high-energy ions penetrating amorphous solids and dissipating their energy in the electronic stopping power regime, cause a permanent expansion perpendicular to the ion track and a contraction parallel to it. If, however, these solids are bombarded in their crystalline forms, no dimensional changes take place.

This phenomenon is not understood, but it is very much related to the mechanical action produced by the secondary electrons produced in conjunction with the electronic stopping power that is also the cause of the fission-fragment ejecta from fissile materials. High-energy cosmic rays have also been implicated in the processing of interstellar dust particles. The attrition, taking place over several hundred million years, is believed to be caused in part by electronic sputtering. By quantifying this process and putting it on a firm physical base, we hope to contribute to the resolution of these scientific issues.

Of more practical interest to LLNL, fission fragment sputtering is likely responsible for the unexplained dispersion that occurs in high activity actinide materials. For example, it has long been known that ^{238}Pu migrates much more rapidly than ^{239}Pu . This is attributed to the higher activity of ^{238}Pu , but the mechanism has never been understood. Sputtering by spontaneous fission and, to a lesser extent, by alpha decay will create ejecta and therefore contribute to the migration of these materials. This is an important consideration in contamination control when handling these materials.

This project was funded at 160K for FY04 and at 226K for FY05. The project was not funded in FY06. As a result, the experimental work and modeling was not completed. However, sufficient experimental and modeling progress was made to answer (or bound) many of the questions that were posed at the beginning of the project.

Background

The fission reaction produces two products with average mass numbers around 97 and 140 and with a total kinetic energy of about 167 MeV. The heavy fission product carries off around 67 MeV while the light fragment has an energy of around 100 MeV. The remainder of the energy liberated by the fission event, about 37 MeV, is imparted on the neutrons (5 MeV), photons (12 MeV), electrons (8 MeV), and neutrinos (12 MeV).

The range of fission products has been measured in U at its normal density of 18.7 g/cc, and it ranges from 4.5 to 7.3 μm , with an average value is 6.7 μm . Since the range varies inversely with the density, the average range in delta Pu can be estimated to be about 7.6 μm .

Sputtering is normally thought of as a knock-on process that is dominated by nuclear interactions of relatively low energy and can be modeled with existing molecular

dynamics codes such as MDCASK. In the energy range of the fission fragments, however, interactions occur largely with the electrons and not with the nuclei. Thus, the sputtering observed is not a result of simple knock-on processes and a more advanced theoretical basis, valid under a wide variety of conditions, is needed. Irradiation experiments provide the necessary hard data to validate the models and refine the fundamental theories and parameters needed to extrapolate to other conditions of interest with confidence. Crucial to this effort will be the development and validation of a theory that accurately models the energy deposition profile of hot secondary electrons that are produced by the fission fragment ion track and an understanding of how the hot secondary electrons impart their energy to the atoms of the matrix.

The fission events occurring within this range from the surface have a probability of 1/4 to emit fission fragments. Along their track, however, the fission fragments produce many recoil atoms with significant kinetic energies that they can also escape. The more detailed analysis of the collision cascades produced by energetic ions gives the following picture. At the end of the range of the energetic ion, a dense collision cascade is produced which resembles a liquid inclusion under high pressure. When this dense collision cascade is close to the surface or even intersects it, part of the heated material can be ejected. Experiments reported in the literature and discussed below have shown that about 1500 atoms are ejected from a U foil per escaped fission fragment, and about 3500 from a Pu foil (see **Table 1**).

The first experimental results reported were by Laptev and Ershler [4]. The experimental setup consisted of a foil of fissile material and a collector foil of aluminum spaced 1 mm apart. The sandwich was enclosed in an evacuated capsule which was inserted in a nuclear reactor and exposed to the thermal neutron flux. After the irradiation, the α activity of the collector foil was measured and the amount of deposited fissile material determined. Some of the results are listed in the table below. They are for the mechanically polished foils with little or no oxide films. Foils with substantial oxide films were reported to have sputtering yields lower by a factor of 100.

Table 1. Number of fissile atoms sputtered per fission fragment escaped from the surface.

Fissile Metal	Neutron Fluence Neutrons/cm ²	Escaped Fission Fragments Fission Fragments/cm ²	Sputtering Yield
²³³ U	2.48*10 ¹⁵	2.00*10 ¹²	550
²³³ U	1.51*10 ¹⁵	2.17*10 ¹²	1000
²³³ U	1.10*10 ¹⁵	1.67*10 ¹²	780
²³³ U	0.45*10 ¹⁵	0.68*10 ¹²	2200
²³⁹ Pu	0.21*10 ¹⁵	0.38*10 ¹²	3990
²³⁹ Pu	1.98*10 ¹⁵	0.33*10 ¹²	2500
²³⁹ Pu	0.16*10 ¹⁵	0.23*10 ¹²	4100

These first results reported by the Russians were followed by experiments on U at Harwell by Rogers and Adam [5]. In these experiments, particular attention was paid to the time dependence of the sputter-deposited material. It was found that the amount of material captured on the collector foil reaches a saturation value with increasing time or fluence because the deposited fissile material will be back-sputtered to the U foil. Therefore, only the initial rate of material collected provides the correct sputtering yield. This yield agreed with the earlier Russian results of about 2000 atoms per escaping fission product. To explore the mechanism of fission fragment sputtering in more detail, Rogers [6] examined by electron microscopy the morphology of the deposits. For low fluences, the deposits consisted of isolated spots containing on average about 10^4 U atoms and forming islands with an average diameter of 7.3 nm. The number of spots increased with fluence until their density reached a value of $3 \times 10^{11} \text{ cm}^{-2}$. Beyond this density, larger islands are formed by spot coalescence. Given the size of the individual deposits, about 10^4 atoms, it was concluded that only one in 16 fission fragments that escaped created a deposit.

While there has been an enormous amount of experimental and theoretical research in subsequent years on implantation sputtering [7,8], no further investigations have apparently been conducted on sputtering from internally generated decay products. However, the knowledge accumulated on implantation sputtering can be applied to the fission fragment sputtering to address the following issues.

a) Temperature Dependence

The dominant mechanism for sputtering at high particle energies and in high-Z materials is by the thermal spike process. Near the end of the energetic particle range, a dense collision cascade is formed which quickly becomes a molten inclusion. However, the duration of the liquid state is so short, on the order of a few picoseconds, that ballistic and diffusional mass transport processes are not affected. It is for this reason that sputtering yields have been found to be independent of the target temperature [9]. It can therefore be assumed that the fission fragment sputtering yields are the same for all temperatures, and even the same for the solid and liquid phases.

b) Surface Conditions

While the early Russian results gave dramatically different results for the sputtering yields of oxidized foils (about 30 fissile atoms per escaped fission fragment) and polished foils, the oxide layers were presumably rather thick. In contrast, Rogers and Adam [5] did not detect any difference in sputtering yields from oxide free or oxidized samples. The oxide film in their specimens were presumably much thinner.

The surface preparation of samples for sputtering experiments has been reported to influence occasionally the measured yields. This has been attributed to “chunk” emission [10] of micron-sized particles which apparently had not been completely removed from the surface during the sample preparation. These particles are believed to have been created by the mechanical polishing process, and they may be released when a collision

cascade forms within it or in close proximity. Obviously, most of these “chunk” emission results have been impossible to reproduce in other experiments.

Approach

The objectives of this LDRD study were as follows:

- verify the sputtering yield that was determined in previous studies
- determine the energy of the sputtered particulate ejecta
- develop a model to explain the observed energy and yield of the ejecta, and
- apply the model to other conditions of interest

To complete the above objectives a combined and integrated approach involving experiments and modeling was pursued. Two types of experiments were pursued, reactor irradiation and accelerator experiments. Modeling was performed using fundamental physics considerations and molecular dynamics codes such as TRIPOS-E and MDCASK.

The first type of experiment was reactor irradiation experiments using natural uranium foil. Natural uranium was used because it is easier to handle than weapons grade plutonium or highly enriched uranium. Natural uranium still has 0.7% ^{235}U and will exhibit about 1/85 of the number of fission fragments as 93% enriched HEU.

The second type of experiment was accelerator experiments using 20 MeV charged Xe^{+5} ions through a foil of tin (Sn). The disadvantage of the accelerator experiments was that the ions have lower energies than the fission induced fragments. However, the accelerator experiments have the advantage that the direction of the beam can be controlled. Another advantage of the accelerator experiments is that non-radioactive samples can be used and no radioactivity is induced by the exposure.

For the modeling portion of the studies, TRIPOS-E was used to model and track the secondary electrons. The code was modified to keep track of the energy and momenta of the individual secondary electrons. MDCASK was then used to model the movement of the nuclei after addition of initial momentum.

Experimental Studies

A. Reactor Irradiations

Specially designed experimental packages were irradiated at the McClellan Nuclear Radiation Center (MNRC). Meeting severe space and materials constraints, these packages contained the uranium foils, the TEM collection grids, and varying pressures of stopping gas. Due to activation related concerns at the MNRC, the materials and quantities in the sample assembly was restricted. The materials allowed for the assembly were carbon-coated titanium for the TEM grids, 1100 series aluminum for the target and sample holder, and a quartz containment vessel which would encapsulate the uranium as well as serve as the vacuum vessel for the less-than-atmospheric-pressure stopping gas. These materials presented construction challenges as titanium TEM grids are a special order item, 1100 aluminum is difficult to precision machine, and quartz glass blowing was no longer available at LLNL. In addition, it was initially agreed that the experiments

would be moved in and out of the reactor using the MNRC’s pneumatic transfer (rabbit) system. This placed further constraints on the design of the experimental package as it could be no larger than 16 mm in diameter and 8 cm in length.

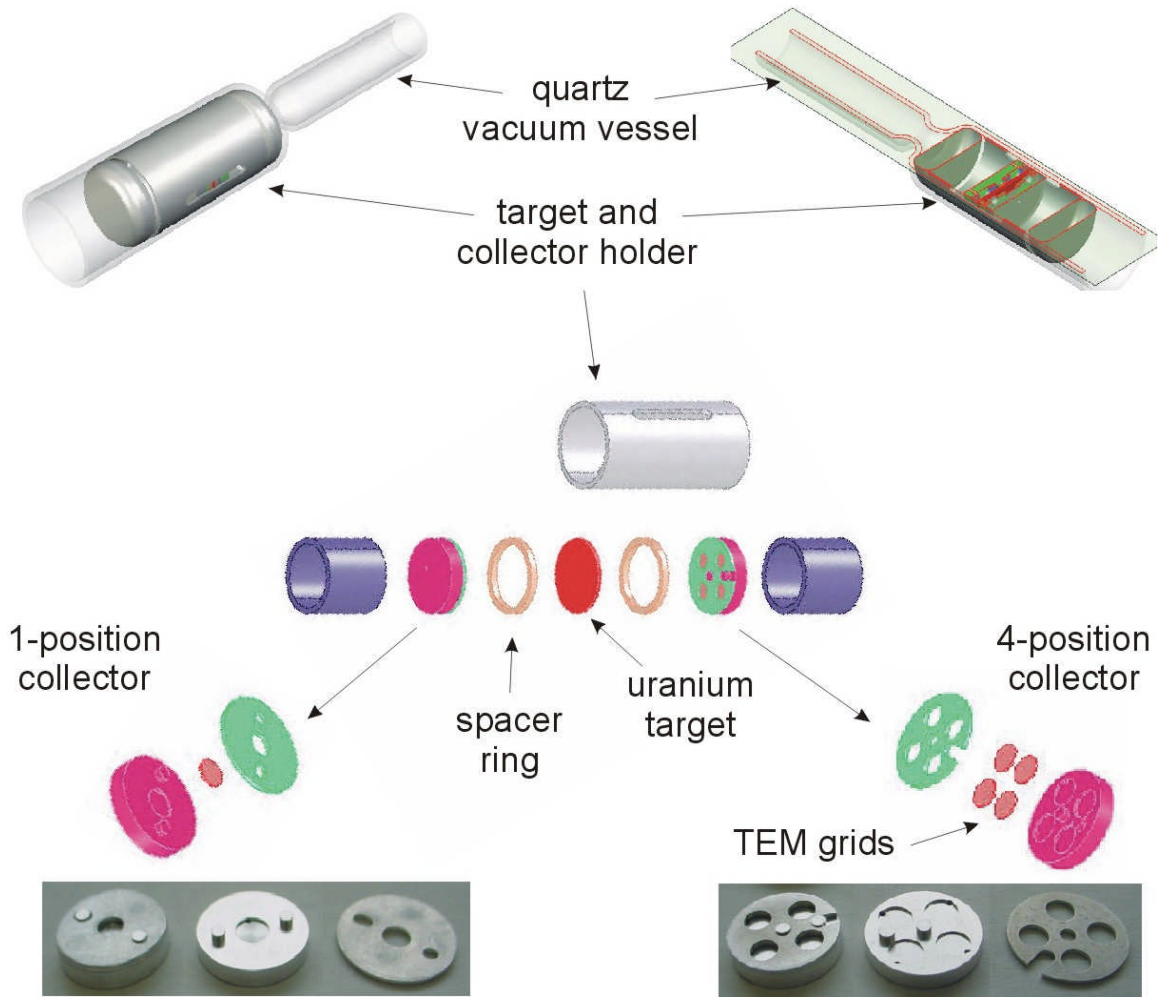


Figure 1. Solid Works design of experimental assembly and images of actual single-place and four-place TEM collector grid holders.

The final design was produced using solid works software and is shown in **Figure 1** along with photographs of some of the parts.

The experiment consists of a 0.33 g disc of natural uranium (11 mm diameter) placed between two spacer rings of identical length. The length of these spacer rings, in conjunction with the pressure chosen for the backfilled gas, provides a scalable resistance to an ejected fission fragment’s flight to the collector grids. This provides flux vs. penetrated gas thickness data similar to that presented by Pauker and Steiger-Shafir for Cf [11] and, when combined with fragment size analysis from the TEM, will set the minimum energy with which the fragments leave the uranium surface. Space limitations did not allow for both on-center and off-center TEM grids to be placed on a single collector. As a compromise, an on-center grid was placed on one side of the uranium

disk, while four off-center collectors were placed on the other. It is hoped that this geometry will allow us to see any angular distribution of the fragment material if it exists. **Figure 2** shows the components of the sample holder prior to assembly. In this picture the uranium disk has been replaced with aluminum disks of an equivalent weight for a test run of the entire package in the reactor at MNRC. **Figure 3** shows the complete assembly of the components from **Figure 2**. **Figure 4** shows the final sealing of the experimental package. Any backfilling of a stopping gas into the evacuated ampule is done just prior to this final sealing step.



Figure 2. Sample holder prior to assembly.

Figure 5 shows the preparation of an ampule from quartz tube stock. This glass blowing capability had been lost from LLNL and had to be reacquired through training sessions with an outside contractor. The sealed ends need special care as any leak would admit air into the experimental package and structural flaws could lead to failure of the vessel during the rapid acceleration and deceleration phases experienced in the pneumatic transfer system. **Figure 6** shows the final experimental assembly. This assembly would



Figure 3. Sample holder after assembly.

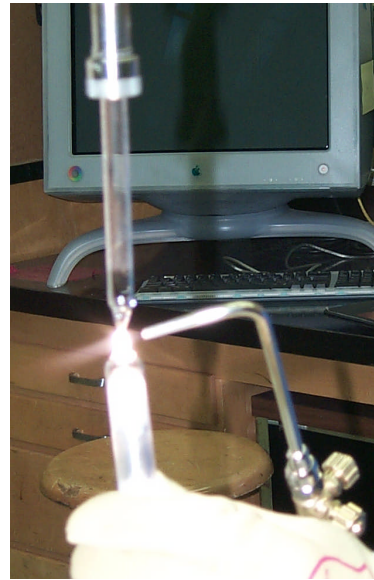


Figure 4. Sealing of sample holder into a quartz ampule.

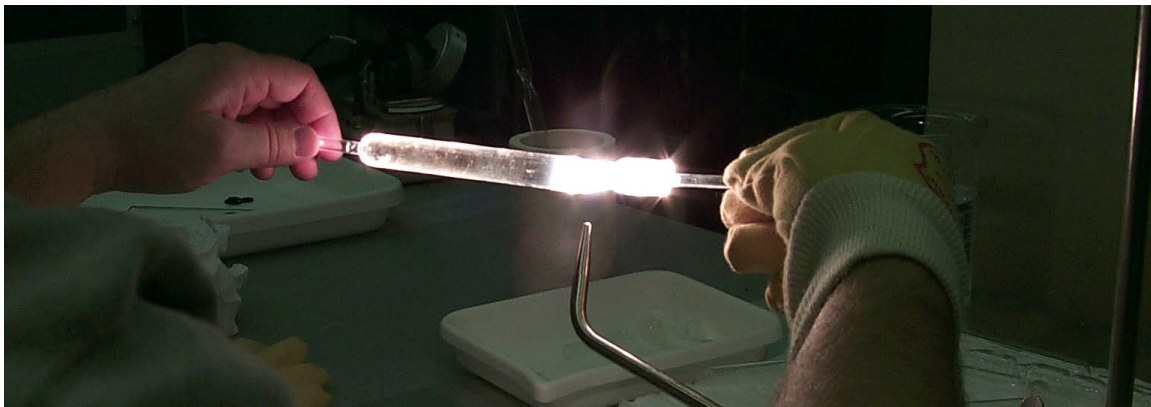


Figure 5. Preparation of quartz ampule from tube stock.



Figure 6. Complete experimental package.



Figure 7. Entire experiment must fit into MNRC "rabbit."

then be placed into a “rabbit” (**Figure 7**) and placed into the pneumatic transfer system at the MNRC for insertion into the reactor. The glass wool seen on either end of the assembly in **Figure 6** prevents the aluminum holder from directly striking the sealed ends of the ampule during acceleration/deceleration. Cushioning material was also placed in the rabbit to prevent the package from moving within the rabbit as well.

Twelve experiments were irradiated at the MNRC. The dose received, the date irradiated, the stopping gas pressure, and other parameters for each experiment can be found in **Table 2**.

TEM analysis of the fission fragments collected on the grids will provide distributions of the fission-induced fragment size, yield, and energy.

Table 2. Summary of irradiation parameters.

Experiment ID (Casing Label)	Irradiation date	Dose	Pressure	Distance U foil to C catcher	U foil thickness	U foil mass
H	9/29/2005	9.60×10^{13}	Vacuum	5 mm	0.008 in	0.32 g
Unmarked	9/28/2005	8.77×10^{14}	Vacuum	5 mm	0.008 in	0.32 g
D	9/9/2005	8.83×10^{15}	Vacuum	5 mm	0.008 in	0.32 g
I	9/29/2005	9.69×10^{13}	1 torr - He	5 mm	0.008 in	0.32 g
F	9/28/2005	8.64×10^{14}	1 torr - He	5 mm	0.008 in	0.32 g
A	9/9/2005	8.94×10^{15}	1 torr - He	5 mm	0.008 in	0.32 g
J	9/29/2005	9.60×10^{13}	10 torr - He	5 mm	0.008 in	0.32 g
G	9/28/2005	8.77×10^{14}	10 torr - He	5 mm	0.008 in	0.32 g
B	9/9/2005	8.69×10^{15}	10 torr - He	5 mm	0.008 in	0.32 g
K	9/29/2005	9.60×10^{13}	100 torr - He	5 mm	0.008 in	0.32 g
C	9/28/2005	8.65×10^{14}	100 torr - He	5 mm	0.008 in	0.32 g
E	9/9/2005	8.88×10^{15}	100 torr - He	5 mm	0.008 in	0.32 g

After approximately half of the experiments had been assembled, evacuated, backfilled, and sealed it was noticed that some of the uranium disks had a shiny residue that adhered to one side. Scraping this residue could remove some material, but it would not delaminate intact. The residue is likely some of the cleaning compound left over from the machining of the material into disks, but will have an unknown effect on the experiments. The residue was only found on a single side, therefore, even if the residue would prevent a fission fragment from reaching a collector, the collector facing the opposite side of the disk should not be affected. It is clearly important to note the relative orientation of the disk and collectors when the experiments are disassembled. If the residue vaporized during irradiation, it will have increased the background pressure inside the tube. This would affect sample collection on both collectors and since no baseline exists, it would be difficult to differentiate from the intentionally backfilled gas pressure.

B. Accelerator Experiments

Simulated fission fragments were generated using the CMS accelerator in B235. In this experiment, 20 MeV Xe^{+5} ions were directed into tin (Sn) foils in both transmission and grazing geometries (**Figure 8**). Tin was chosen as a non-radioactive surrogate for uranium based upon a figure-of-merit (FOM) derived from a ratio of its electronic stopping power (for ion energies near the surface) to its melting point. In a transmission geometry (in which the Xe ions enter a 1 μm thick foil with 20 MeV and exit with ~ 8 MeV) the FOM for Sn is ~ 0.833 . Using this FOM scheme, a Sr fission fragment within uranium has an FOM of ~ 2.083 , just 2.5 times greater than the FOM for Sn. Other potential surrogates scored a little lower using this FOM: 0.800(Cd), 0.693(In), 0.684(Pb), and 0.664(Zn). The similarity in magnitude of the FOM suggests that ejecta produced by these materials may originate via the same mechanism. It is for this reason that accelerator driven ions can provide additional test data for calculations designed to simulate fission-induced ejecta.

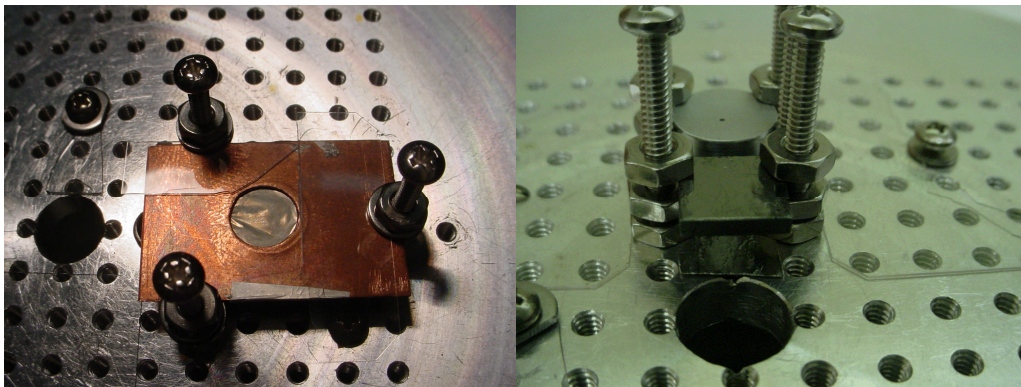


Figure 8. Accelerator driven fission fragment simulations using transmission (left) and grazing incidence (right) geometries. Three substrates are present in the grazing geometry: TEM grid (top, circular), Si (middle, not visible), and highly-ordered pyrolytic graphite, HOPG (bottom black square). The three samples are used in TEM, AFM, and RBS measurements, respectively.

The transmission geometry experiments were inconclusive because only one Sn fragment was collected, well below our initial expectation. The beam dose required to determine the sputter rate is much higher than we used but appears to be easily achieved with our present set-up. **Figure 9** shows TEM images of a sputtered fragment collected from a foil in the transmission geometry.

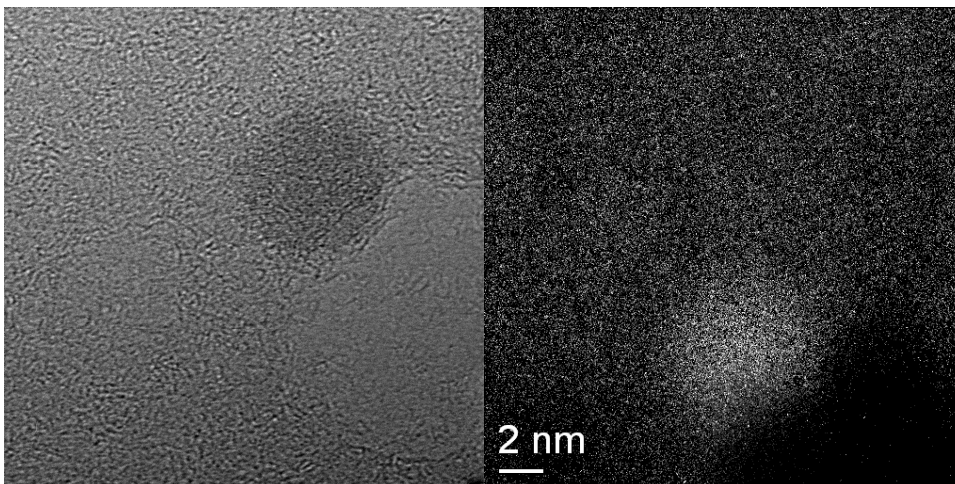


Figure 9. TEM image (left) and Jump Ratio image (right) of a Sn particle sputtered from a transmission geometry accelerator experiment.

Multiple fringe sets in the left image show that the particle is polycrystalline, while the pattern produced in the jump ratio image on the right confirms that the particle is Sn. The featureless area below and to the right of the particle in both images is likely the damage track left by an ~8 MeV Xe ion in the collection foil.

Total fluence for the experiment was 4.44×10^{12} Xe/cm². Only this one particle was found upon searching two TEM grids ($\sim 3.25 \times 10^4$ μm^2). Assuming it is a hemisphere, it contains ~ 1200 atoms.

Our simulations indicated that the amount of energy transferred from the passing ion would be greater in the radial direction than in the axial direction. Our results of the grazing angle geometry experiment confirm the modeling. **Figure 10-left** is a TEM image of the particles collected from the grazing geometry. Two particles, with crystalline fringes, are clearly seen in the lower left quadrant of the image. Several even smaller particles seem likely. Unlike the TEM analysis for the transmission geometry, these particles were found very quickly after examining a limited region. However, there were still too few particles to accurately determine a particle density using TEM. An EDX analysis (**Figure 10-right**) of the area shown in **Figure 10-left** indicates that the particles are, in fact, Sn and not some other contaminant.

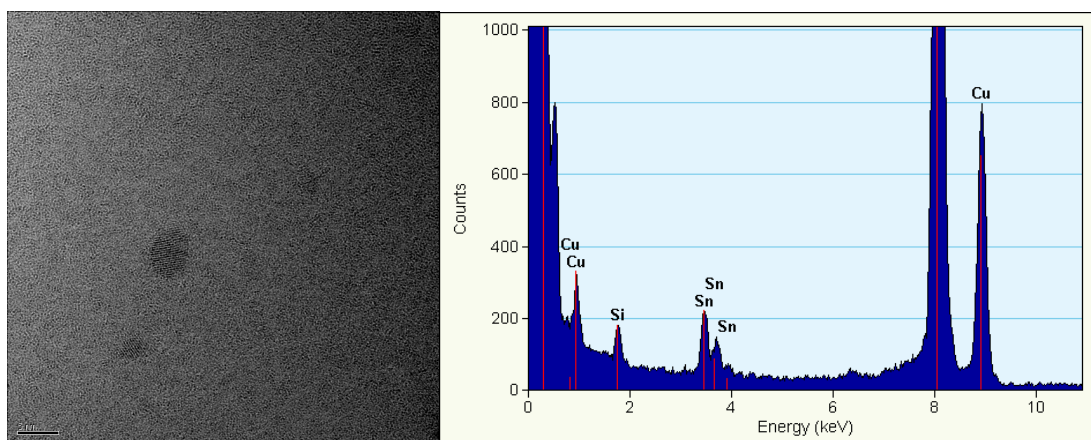


Figure 10. TEM image (left) and EDX analysis (right) of particles sputtered using 20 MeV Xe⁺⁵ ions at grazing incidence. The legend bar in the lower left of the TEM image is at 5 nm.

During the grazing geometry experiment it was possible to simultaneously collect the sputtered Sn on substrates suitable for AFM analysis. **Figure 11-top and lower left** show AFM images of Sn which was co-deposited onto the Si substrate. A large number of particles are seen in these images, and although the AFM has no mechanism to conclusively prove that the particles shown are Sn, the image of the clean substrate (**Figure 11-lower right**) shows that the particles seen can not be accounted for by pre-existing contamination. In addition, Rutherford Backscattering from the highly ordered pyrolytic graphite (HOPG) substrate (see **Figure 8**) showed a surface concentration of Sn atoms at $\sim 10^{15}$ atoms/cm². The incoming Xe ion flux for these substrates was $\sim 1.5 \times 10^{13}$ Xe/cm².

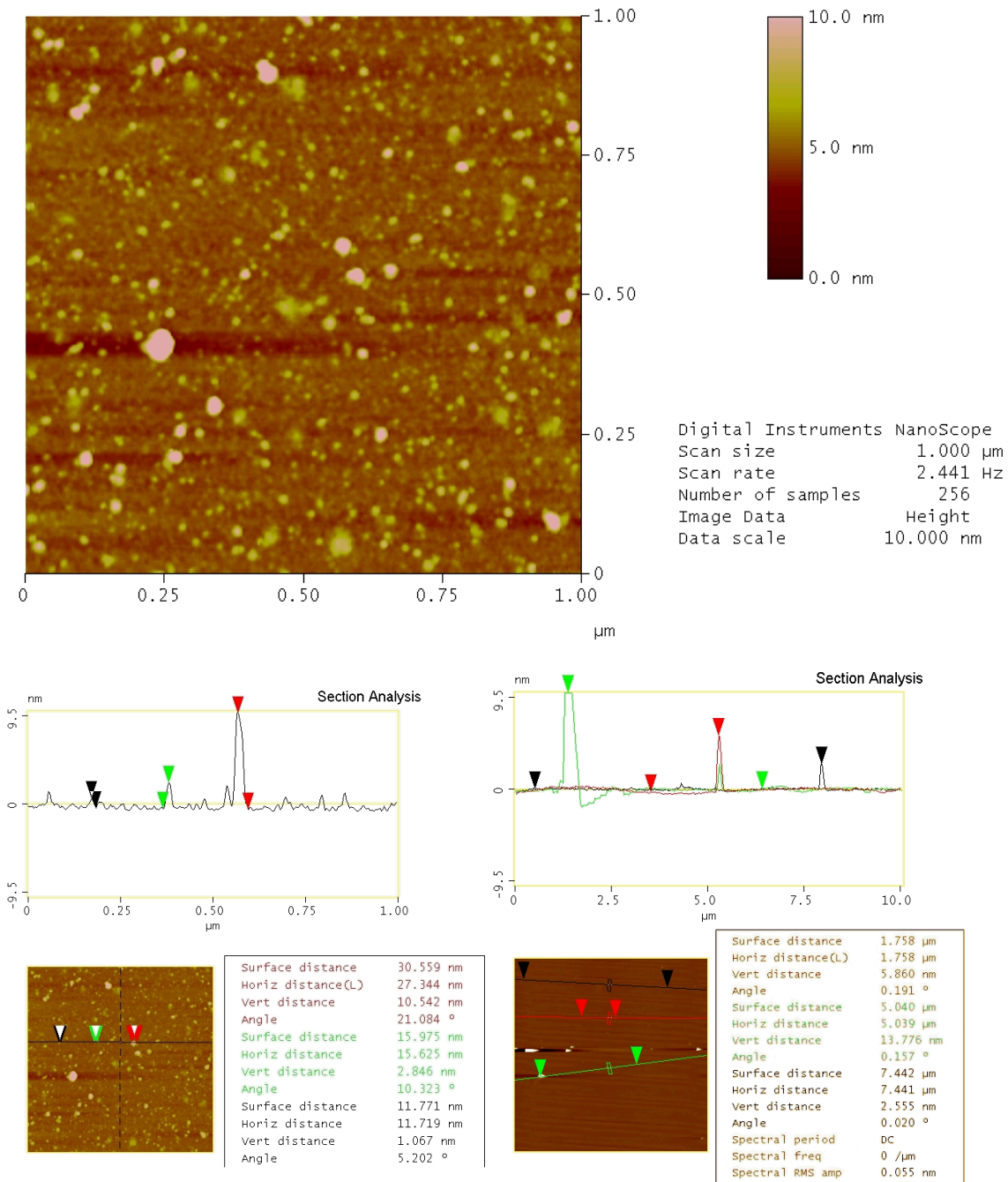


Figure 11. AFM images of grazing angle sputtering experiments. AFM image (top) and sectional analysis (lower left) of deposition substrate. Sectional analysis of a clean Si substrate (lower right) shows that most of the features seen in the AFM image are not due to pre-existing contamination.

If we assume that the particles ejected are hemispheres, that in the metal Sn bonds to neighboring Sn with ~ 1 eV and is separated by about 2 \AA , and that each Sn on the ejected particle breaks only one bond with a Sn atom in the parent material, a maximum ejected particle size can be determined. For 20 MeV a maximum diameter of ~ 600 nm is found, and for 8 MeV, ~ 400 nm. Though the assumptions used are very rough estimates of the

true value, this result is an order of magnitude larger than the measured sizes of any of the particle we have seen, providing further indication that the observed particles are the result of the sputtering process and not the result of contamination.

Modeling Studies

A. Kinetic Energy of the Sputtered Material

Very few studies have been carried out on the energy distribution of sputtered atoms. An example [12] of an energy spectrum from 6 keV Xe⁺ implantation of Ag is shown in **Figure 12**.

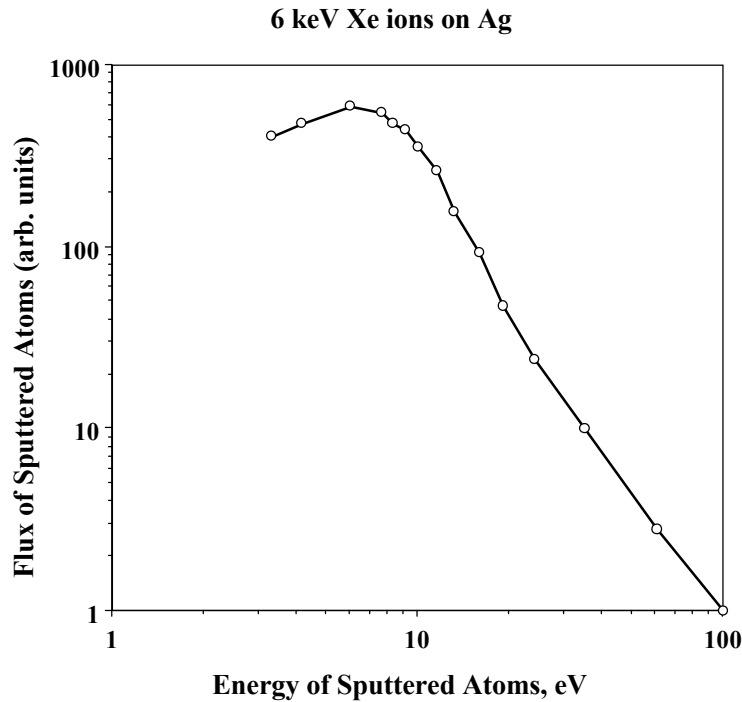


Figure 12. Energy spectrum of Ag atoms sputtered from an Ag target with 6 keV Xe⁺ ion beam.

The energy spectrum can be fitted by a superposition of two spectra.

$$\Phi_{\text{spike}}(E) = C_1 E \exp(-3E/2\Theta) + C_2 E/(E+E_B)^3 \quad (1)$$

The first term represents the atom flux emitted from the thermal spike region of the collision cascade. The mean energy of the atoms in the thermal spike is denoted by Θ , and it is equal to 9 eV for the spectrum shown in **Figure 12**. Much larger values of Θ are expected for high energy, heavy ion damage in high-Z targets. The second term arises from the few target atoms which receive a large momentum transfer from the primary

ion, and it mainly contributes to the high-energy tail of the spectrum. E_B is an effective surface binding energy, and C_1 and C_2 are two fitting parameters.

The material sputtered by low energy ions is in the form of individual target atoms, and their energy distribution as well as the sputtering yield is determined by the nuclear stopping power. For high-energy heavy ions, the electronic stopping power is dominant, and it is not known how the ejected target material acquires its kinetic energy, much less how large it is.

To obtain an estimate for the kinetic energy of ejecta, S. Pauker and N.H. Steiger-Shafir [11] employed low pressure gas as a stopping medium, The emission of Cf ejecta was collected across a gap filled with air at different pressures. The width of the gap was 0.5 cm.

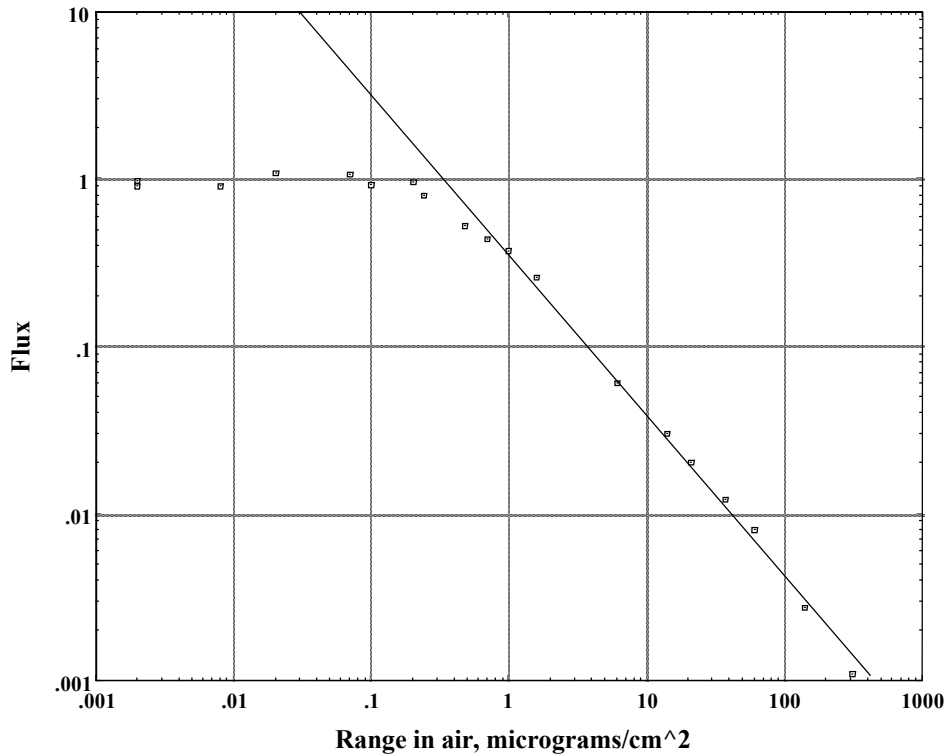


Figure 13. Flux of Cf ejecta as a function of the gas pressure (given as $\mu\text{g}/\text{cm}^2$).

By increasing the air pressure in the chamber, the particle flux is reduced in the manner shown in the figure. It is seen that the range of the particles is obtained by the break in the flux curve, and it is at $0.32 \mu\text{g}/\text{cm}^2$. To relate the air thickness to an actual length R and to a pressure p , we note that at room temperature

$$\begin{aligned}
 R_{eq} [\mu\text{g}/\text{cm}^2] &= 10^6 R[\text{cm}] n[\text{cm}^{-3}] m_{amu} M \\
 &= R[\text{cm}] p[\text{torr}] 1.753
 \end{aligned}
 \tag{1}$$

Here, n is the number of air molecules per cm^3 , M is the molecular weight of a molecule (assumed to be 28.8 for air), and m_{amu} is the atomic mass unit.

The pressure required to reduce the actual range to 0.5 cm is found to be 0.41 torr. The mean free path of the gas molecules at room temperature is

$$\lambda = 5 \cdot 10^{-3} / p[\text{torr}] = 0.0146 \text{ cm}. \quad (2)$$

Assuming that the ejecta particles have a radius of $r_p = 10 \text{ nm}$, we have a Knudsen number of $\lambda/r_p = 10^5$. Accordingly, the drag exerted on the particle by the gas molecules is not given by the Stokes equation, but by the following equation for free molecular drag [13]

$$D = \frac{8}{3} r_p^2 n \sqrt{2\pi m_G kT} \left[1 + \frac{\pi}{8} \alpha_m\right] V. \quad (3)$$

Using the following values for

$$\begin{aligned} \text{the gas density } n_G &= 1.34 \cdot 10^{16} \text{ molecules/cm}^3, \\ \text{the accommodation coefficient } \alpha_m &= 1, \\ \sqrt{2\pi m_G kT} &= 3.49 \cdot 10^{-19} \text{ g cm / s} \end{aligned}$$

one obtains

$$D = 1.73 \cdot 10^{-16} r_p^2 [\text{nm}] V [\text{cm / s}] = \Theta V \quad (4)$$

where V is the particle velocity. The slowing-down of the particle in the gas is described by the equation of motion

$$M_p \frac{dV}{dt} = -\Theta V \quad (5)$$

and has the solution

$$V(t) = V_0 \exp[-\Theta t / M_p], \quad (6)$$

where V_0 is the initial velocity. The actual range of the particle is now obtained as

$$R = \int_0^{\infty} V(t) dt = V_0 \frac{M_p}{\Theta}. \quad (7)$$

Next, we write for the particle mass

$$M_p = \rho \frac{4\pi}{3} r_p^3 \quad (8)$$

and insert this into equation (7). Using the definition for Θ from eq.(4) and the actual range of $R = 0.5$ cm, we finally obtain

$$\rho [g/cm^3] r_p [nm] V_0 = 2069. \quad (9)$$

Assuming a density of 10 g/cm³ for Californium oxide and a particle radius of 10 nm, an initial velocity of 20.7 m/s is found. This corresponds to an average kinetic energy of 56.0 eV.

B. Theory of Energy and Momentum Distribution

The loss of energy of a charged particle in matter can be divided into three contributions. At very high particle velocities greater than the orbital velocity of bound electrons in the atoms of the stopping medium, the energy loss is due mainly to collisions with the electrons in the stopping medium and also due to the production of photons at relativistic velocities. At lower particle velocities, the charged particle transfers momentum directly to the atoms. The rate of energy loss of the incident ion consists then of the electronic, the radiative, and the nuclear stopping power. Traditionally, only the latter is considered to produce mechanical effects in the stopping medium such as atom displacements and structural defects, while the electronic and radiative losses are assumed to be converted to heat in the stopping medium. This conversion to heat is mediated by the secondary electrons and photons ejected from atoms of the stopping medium and subsequently absorbed within this medium but at locations away from their points of origin. The spread of this energy, mainly by the secondary electrons, creates the so-called ion track. In certain materials, the deposited energy results in subtle structural or chemical changes which can be revealed afterwards by preferentially etching away the altered material.

The spatial extent of the energy deposition from the secondary electrons has been of particular importance for water and for biological tissues to assess the biological effectiveness of nuclear radiation from different sources as it affects living organisms. These studies have shown that the ion tracks have diameters ranging from a few nanometers in heavy metals to micrometers in polymers and biological tissue. The great majority of secondary electrons receive modest to small amounts of kinetic energy, and its subsequent dissipation to the atoms in the track region imparts an even smaller impulse. It is perhaps not surprising that it has generally been assumed that the electronic energy loss of charged particles produces no mechanical effects in the stopping medium other than heat, *i.e.*, an increase in the random motion of its atoms.

In the following section, we develop the theory for deposition of linear momentum and for energy imparted by the secondary electrons to the target atoms within the ion track. The theoretical derivation follows the model for the energy deposition developed by Kobetich and Katz [14] and others. In particular, the model of Kiefer and Straaten [15] is employed. This model uses a simple analytical formula for the penetration and range of energetic electrons in matter. The simple, analytical expressions thereby obtained contain

the essential physics in a tractable form suitable for further applications. For example, the mechanical forces created in the ion track can be incorporated in a molecular dynamics code to perform large-scale atomistic simulations of the mechanical response of metals subject to high-energy, charged particle irradiations.

C. Impact produced by Energetic Ions on Matter

Let us first consider a simple case of a projectile of mass m and initial velocity v impacting and becoming embedded into a solid target of mass M ; the target is initially at rest. Conservation of linear momentum demands that the velocity V of the target and the embedded projectile be given by

$$V = \frac{m}{M + m}v \quad (10)$$

The kinetic energy of target and projectile after impact, E_t , is then

$$E_t = \frac{m}{M + m}E_p \quad (11)$$

where E_p is the initial kinetic energy of the projectile. The internal energy of the combined target and projectile, U , has increased by the amount

$$U = E_p - E_t = \frac{M}{M + m}E_p \quad (12)$$

This internal energy increase has in general many contributions: thermal energy, energy stored in dislocations and twins produced by the plastic deformation, enthalpy of transformation associated with new phases created by the transient pressure rise, and surface energy of the internal cracks and cavities formed during the deformation.

It is important to realize that both the internal energy and the mass M of a large target are not immediately affected at the moment of impact. Rather, only a small fraction of the mass M is initially accelerated and receives kinetic energy in the collision. This kinetic energy is subsequently shared with the remaining target mass by propagating shock and elastic waves spreading from the site of impact. Eventually, these propagating waves reflect from other parts of the target surfaces and are dampened by dissipative processes which convert their energy into heat, crystalline defects, and rupture surfaces.

During this gradual conversion, the target mass which is put into motion grows from the initial small amount, ΔM , composed of the atoms in direct contact with the projectile, to the entire mass M of the target.

Our aim in this paper is to determine ΔM as well as the associated impact forces for the case that the projectile is a high-energy, heavy ion penetrating a slice of matter while losing part of its energy through the electronic stopping power. If we denote this loss of projectile energy by ΔE_p , then the target mass ΔM receives from the projectile the kinetic

energy component associated with the motion parallel to the projectile trajectory, henceforth called the axial or z -direction,

$$\Delta E_z = \frac{m_p}{\Delta M} \Delta E_p \quad (13)$$

Note, that the projectile mass m_p is not added to ΔM in the denominator of equation (13), in contrast to equation (12), since the ion exits the slice of matter with thickness Δx . Dividing equation (13) by this thickness leads to

$$\frac{\Delta E_p}{\Delta x} = \frac{\Delta M}{m_p \Delta x} \Delta E_z = \frac{\pi R^2 \rho_M}{m_p} \Delta x 2\pi \int_0^R \Delta e_z(r) r dr \quad (14)$$

The last part of equation (14) is obtained by first assuming that the target volume impacted by the projectile ion is equal to $\pi R^2 \Delta x$ and that the target mass density is ρ_M . Second, we acknowledge that the kinetic energy is imparted on this target volume in a non-uniform manner expressed in the form of a kinetic energy density $\Delta e_z(r)$ per unit volume. However, we suppose that this kinetic energy density depends only on the radial distance r measured from the trajectory of the ion, and that it extends to a maximum distance R , the radius of the ion track.

We express the kinetic energy density in the same manner as in fluid dynamics, namely as

$$\Delta e_z(r) = \frac{1}{2} \rho_M \Delta v_z^2(r) \quad (15)$$

where $\Delta v_z(r)$ is the increment of the target atom flow velocity component parallel to the ion track. Obviously, there will also be a radial component $\Delta v_r(r)$ and an associated kinetic energy distribution $\Delta e_r(r)$. Since the transfer of energy and linear momentum to target atoms is mediated by the electron shower produced by the projectile ion, the ionized and excited target atoms within the ion track will have absorbed an amount of energy, ΔU_e , in addition to the mean excitation energy, ΔU_I , produced directly by the projectile ion.

Conservation of energy leads then to the relationship

$$\frac{\Delta E_p}{\Delta x} = \frac{\Delta U_I}{\Delta x} + \frac{\Delta U_e}{\Delta x} + 2\pi \int_0^R (\Delta e_z + \Delta e_r) r dr \quad (16)$$

Equations (14) and (16) can be solved for the parallel and radial contributions of the kinetic energy imparted on target atoms, with the result that

$$2\pi \int_0^R \Delta e_z(r) r dr = \frac{m_p}{\pi R^2 \Delta x \rho_M} \frac{\Delta E_p}{\Delta x} \quad (17)$$

$$2\pi \int_0^R \Delta e_r(r) r dr = \left(1 - \frac{m_p}{\pi R^2 \Delta x \rho_M}\right) \frac{\Delta E_p}{\Delta x} - \frac{\Delta U_l}{\Delta x} - \frac{\Delta U_e}{\Delta x} \quad (18)$$

These equations do not determine the actual spatial distribution of the kinetic energy imparted on the target atoms within the ion track column, they only impose global constraints due to the global conservation of linear momentum, equation (17), and energy, equation (18). To obtain the spatial distribution requires both an analysis of the secondary electron spatial and energetic distribution and the electron energy loss and its transmission to the target atoms. This will be done in the following section.

D. Energy Deposition by Secondary Electrons

Let us begin by considering the electrons emitted from one point along the trajectory of the incident ion, assuming that the trajectory is straight at this point. The electrons are emitted at various angles θ from the ion trajectory. If we neglect the initial electron velocity and its binding energy to the atom, then its recoil energy T is related to the scattering angle by

$$\cos^2 \theta = T/T_m \quad (19)$$

for non-relativistic energies $T \ll 2mc^2$. Here, m is the electron mass, c the speed of light, and

$$T_m \approx 4 \frac{m}{M} E = 2mV^2 \quad (20)$$

is the maximum recoil energy imparted by the incident ion of mass M , kinetic energy $E \ll Mc^2$, and ion speed V .

The secondary electrons have a projected range along their initial recoil direction which is given approximately by the empirical formula

$$R(T) = CT^n. \quad (21)$$

A convenient measure for the spatial extent of the secondary electrons is the maximum range

$$R_m = CT_m^n. \quad (22)$$

With it, we introduce dimensionless radial and axial coordinates

$$\rho = r/R_m \quad \text{and} \quad \zeta = z/R_m \quad (23)$$

A secondary electron with recoil energy T will reach its final destination (in an average sense) at the location

$$\rho_m = \left(\frac{T}{T_m}\right)^n \sqrt{1 - \frac{T}{T_m}} \quad \text{and} \quad \zeta_m = \left(\frac{T}{T_m}\right)^{n+\frac{1}{2}} = \cos^{n+\frac{1}{2}} \theta \quad (24)$$

from its point of origin. Along its straight, projected path it will deposit both its energy and linear momentum. At the location $(\rho < \rho_m, \zeta < \zeta_m)$, it will have a residual energy w given by

$$C [w(\rho, \zeta)]^n = R(T) - R_m \sqrt{\rho^2 + \zeta^2} \quad (25)$$

Division of this equation by eq. (21) provide alternate forms, namely

$$\left(\frac{w}{T}\right)^n = 1 - \frac{\rho}{\rho_m} = 1 - \frac{\zeta}{\zeta_m} \quad (26)$$

We employ the second form and use eqs. (19) and (24) together with the definition $\cos \theta = \zeta / \sqrt{\rho^2 + \zeta^2}$ to finally obtain

$$w(\rho, \zeta) = T_m \frac{\zeta^2}{\rho^2 + \zeta^2} \left[1 - \sqrt{\rho^2 + \zeta^2} \left(1 + \frac{\rho^2}{\zeta^2} \right)^n \right]^{1/n} \quad (27)$$

for the residual energy of the secondary electron at the position (ρ, ζ) relative to its point of origin.

This expression needs to be multiplied with the number of secondary electrons emitted at a given angle or a given recoil energy. This number is given by the differential scattering cross section for elastic collisions of the incident ion of effective charge Z^*e with the number density NZ of electrons in the stopping medium, *i.e.* by

$$dn(T) = \frac{2\pi NZ Z^{*2} e^4}{m V^2} \frac{dT}{T^2} = B \frac{dT}{T^2} \quad (28)$$

Using eq.(19) in the form

$$T = T_m \frac{\zeta^2}{\rho^2 + \zeta^2} \quad \text{and} \quad dT = T_m \frac{2\rho^2 \zeta}{(\rho^2 + \zeta^2)^2} d\zeta,$$

this may also be written as

$$dn(\zeta) = \frac{B}{T_m} \frac{2\rho^2}{\zeta^3} d\zeta \quad (29)$$

The product of equation (29) with equation (27) defines now the flux of energy through a cylinder of radius ρ at the axial location ζ as

$$\phi(\rho, \zeta) d\zeta = 2B f(n, \rho, \zeta) \frac{\rho^2}{(\rho^2 + \zeta^2)} \frac{d\zeta}{\zeta} \quad (30)$$

Here, the function

$$f(n, \rho, \zeta) = \left[1 - \sqrt{\rho^2 + \zeta^2} \left(1 + \frac{\rho^2}{\zeta^2} \right)^n \right]^{1/n} \quad (31)$$

is only defined for those coordinate pairs (ρ, ζ) which render it positive, otherwise it must be set equal to zero.

The radial derivative of the flux function (30) determines now the density for energy deposition:

$$Q(\rho, \zeta) = -\frac{1}{2\pi\rho} \frac{\partial\phi}{\partial\rho} \quad (32)$$

We may separate this energy density into an axial and a radial component as follows,

$$Q_z(\rho, \zeta) = Q(\rho, \zeta) \cos^2 \theta = Q(\rho, \zeta) \frac{\zeta^2}{\rho^2 + \zeta^2} \quad (33)$$

$$Q_r(\rho, \zeta) = Q(\rho, \zeta) \sin^2 \theta = Q(\rho, \zeta) \frac{\rho^2}{\rho^2 + \zeta^2} \quad (34)$$

since we approximate the electronic energy loss along a straight projected range. This approximation is further justified by integrating now these energy densities over the axial coordinate ζ .

This integration will then give the energy deposited at a point located at a distance ρ from the projectile ion path. We can easily show this by viewing the situation from a moving coordinate system with the projectile ion at its origin, and the target material streaming past this ion. The secondary ion shower becomes a stationary, but continuously operated source, and the total exposure of a particular target point amounts to axial integration.

The axially integrated functions

$$\bar{Q}_z(\rho) = \int_{\zeta_1}^{\zeta_2} Q_z(\rho, \zeta) d\zeta \quad (35)$$

$$\bar{Q}_r(\rho) = \int_{\zeta_1}^{\zeta_2} Q_r(\rho, \zeta) d\zeta \quad (36)$$

multiplied with $\pi\rho/B$ are shown in **Figure 14**. The integration limits are determined by the solutions of $Q(\rho, \zeta_{1,2}) = 0$.

E. The Impulse Deposition by Secondary Electrons

The energy deposition by the secondary electrons occurs by further ionization and excitation of target atoms and conduction electrons. Subsequent recombination and de-excitation results in electromagnetic radiation, most of which is absorbed by the target material and converted to heat. However, some fraction must result in mechanical impact forces on target atoms within the ion track in order to satisfy linear momentum conservation. We denote this fraction by $F(\rho)$, and equate the product $F(\rho)\bar{Q}_z(\rho)$ with the axial kinetic energy density Δe_z defined in equation (17). This equation then becomes

$$2\pi \int_0^{\rho_m} F(\rho)\bar{Q}_z(\rho)\rho d\rho = \frac{m_p}{\rho_M \pi (\rho_m R_m)^2 \Delta x} \frac{\Delta E_p}{\Delta x} \quad (37)$$

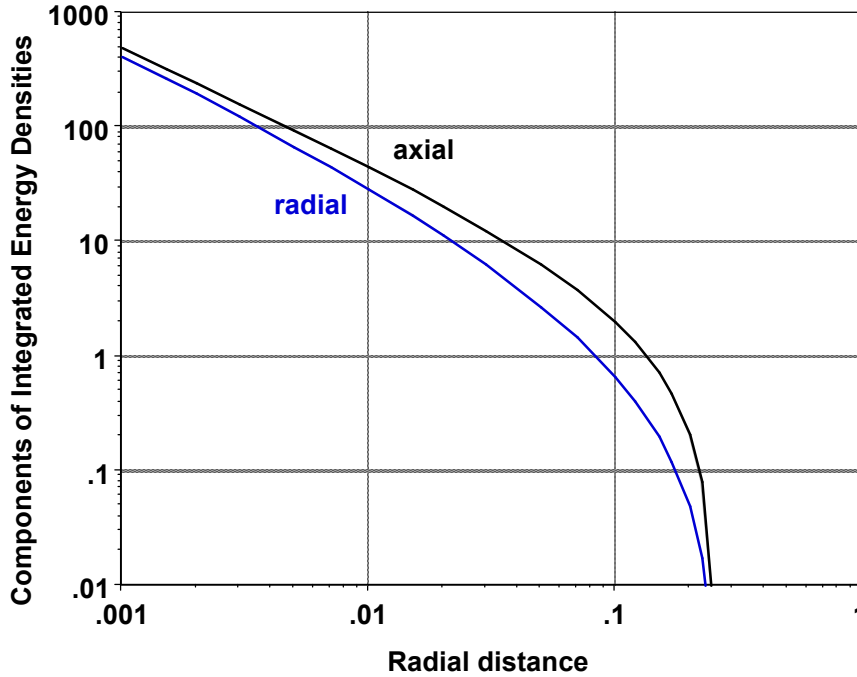


Figure 14. Axial and radial energy density as a function of radial distance.

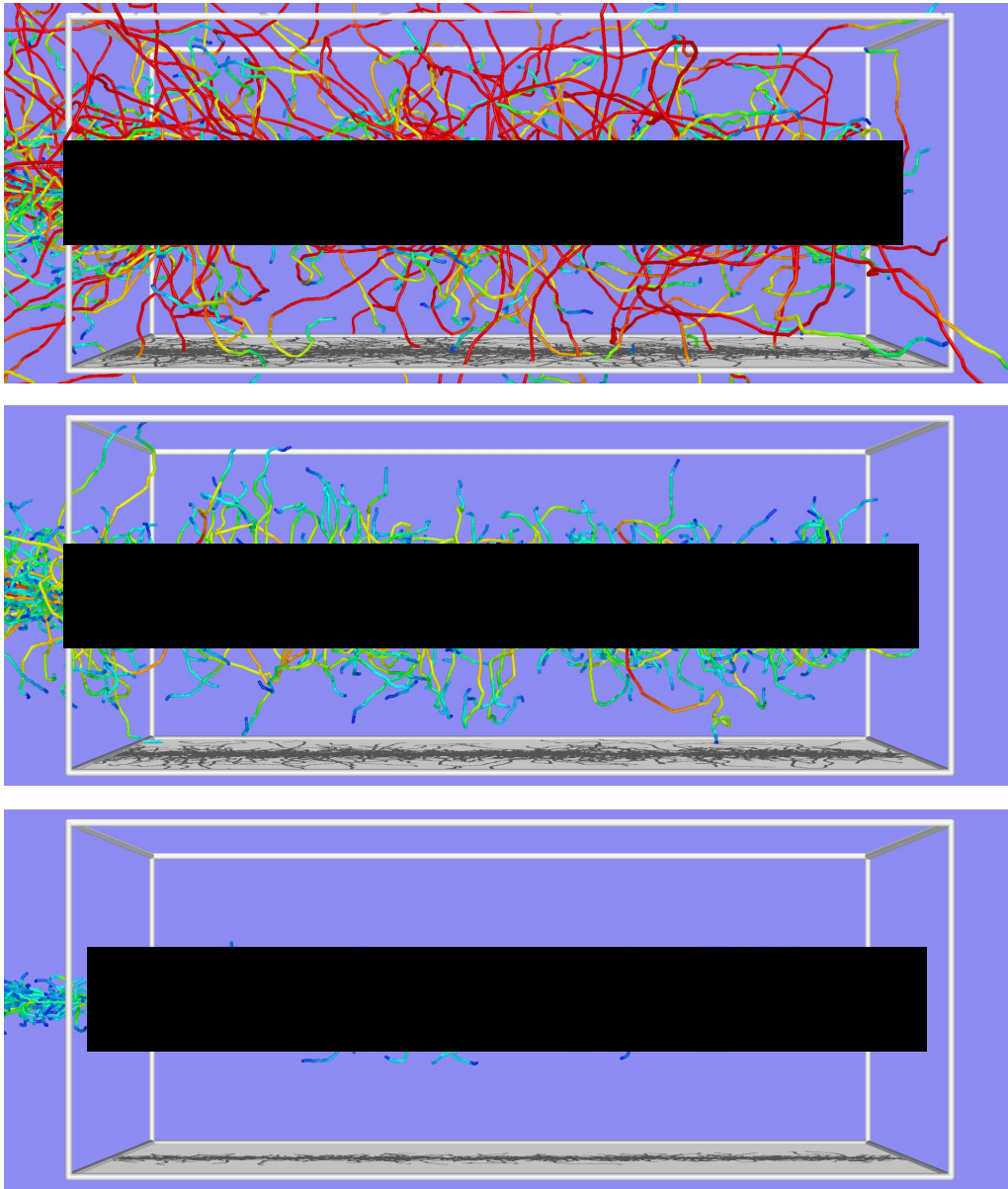


Figure 15. Trajectories of secondary electrons produced by 100 MeV ions in plutonium with the TRIPOS-E code. Top is for ion mass of 180 amu, middle for 120 amu, and bottom for 60 amu. The arrow depicts the path of the ion through a plutonium sample of 250 nm length and 100x100 nm cross section.

F. Monte-Carlo Simulations of Energy Transport

Secondary electron generation and transport along ion tracks was examined with the TRIPOS-E code developed by Martin and Ghoniem [16]. Three examples are shown in **Figure 15**. It is seen that with increasing mass of the projectile ion, the range of the secondary electrons increases, giving rise to a ion track of larger radial extension. It should be noted, that TRIPOS-E only follows the trajectories of the secondary electrons with energies higher than a specified value. Although this value can be chosen in principle to be low, in practice it is not possible to follow low energy secondary electrons since their numbers are excessively large, yet they deposit most of the energy. It is therefore necessary to compute the energy deposition profile with theoretical models such as presented in the previous section.

Exit Plan/ Summary

As stated previously, the experimental and modeling work was not completed. The samples irradiated at the MNRC are on site at LLNL and could be analyzed at any time in the future. The samples are contained in sealed ampoules and should remain in good condition for the foreseeable future.

The accelerator experiments, though insufficient in number to produce solid findings, show great promise of providing a parallel track of study in this area that avoids working with radioactive materials or reactor irradiations. Further experiments could provide valuable tests of the theoretical models. Our present experiments confirm the modeling studies which attribute the sputtering of materials occurs primarily from the fragments produced parallel to the surface rather than perpendicular to the surface. This appears to be borne out by the single grazing incidence experiment that was performed.

As mentioned above, the modeling work that was accomplished under this program was beginning to exhibit some accurate predictive power. Further work, along with the input of additional data, would further refine the model and expand its predictive capability. For example the size distribution and overall yield could be determined experimentally and expand with theory. Since these experiments and theory can be done in both grazing and perpendicular geometries, the distribution of energy radially and axially could be determined. The velocity of the particles could be measured if a suitable gas cell can be designed for use in the accelerator.

As a result of this study, fission fragment sputtering is better understood. Typical sputtering yield is about 2000 atoms per fission fragment. The energy of the ejected particulates (*i.e.* the sputtered material) is around 60 eV. This is a very low energy considering that fission fragments between 60 and 100 MeV are the source behind the sputtered material. The mechanism although not yet fully understood is likely the result of repulsive forces of the nuclei that result from the scattering and ejection of the secondary electrons that interact with the high energy fission fragments. These conclusions provide additional valuable insights into contamination control issues of high activity actinide materials.

References

1. R.L. Fleischer, P.P. Price, and R. M. Walker, "Nuclear Tracks in Solids", Cal. Univ. Press, 1975.
2. S. Klaumunzer and G. Schuhmacher, *Phys. Rev. Letters*, **51**, 1987 (1983).
3. Teun van Dillen, "Ion-irradiation induced anisotropic plastic deformation", Thesis, <http://www.amolf.nl>.
4. F.S. Laptev and B.V. Ershler, "Vaporization of Metals by Fission Products", *Sov. J. Nucl. Energy*, **4**, 513 (1957).
5. M.D. Rogers and J. Adam, "Ejection of Atoms from Uranium by Fission Fragments," *J. Nucl. Materials*, **6**, 182 (1962).
6. M.D. Rogers, "Mass Transport of Uranium by Fission Fragments," *J. Nucl. Materials*, **15**, 65 (1965).
7. "Sputtering by Particle Bombardment I. Ed. by R. Behrisch, Vol. 47 of Topics in Applied Physics, Springer-Verlag, Berlin, 1983
8. "Sputtering by Particle Bombardment II. Ed. by R. Behrisch, Vol. 52 of Topics in Applied Physics, Springer-Verlag, Berlin, 1983
9. J. Bohdanský, H. Lindner, E. Hechtel, A.P. Martinelli, and J. Roth, "Sputtering Yield of Cu and Ag at Target Temperatures Close to the Melting Point", *Nucl. Instr. Methods*, **B18**, 509 (1987).
10. P. Dusza, S.K. Das, and M. Kaminsky, "Neutron Sputtering of Solids", in Radiation Effects on Solid Surfaces, Adv. Chem. Series 158, *Amer. Chem. Soc.*, p.65 1976.
11. S. Paulker and N. H. Steiger-Shafir, "Transfer properties of ^{252}Cf and their use for source preparation," *Nuclear Instruments and Methods*, **91**, 557-563 (1971).
12. M. Szymonski and A.E. De Vries, "Spikes in Low Energy Sputtering of Silver and Gold", *Phys. Letters*, **63A**, 359 (1977).
13. J.R. Brock, *J. Phys. Chem.*, **68**, 2862 (1964).
14. E.J. Kobetich and R. Katz, *Phys. Rev.*, **170**, 391, 397, 401, 405 (1968).
15. J. Kiefer and H. Straaten, *Phys. Med. Biol.*, **31**, 1201 (1986).
16. R.C. Martin and N.M. Ghoniem, *Phys. Stat. Sol. (a)*, **104**, 743 (1987).